Research Article | Vol. 24, No. 20 | 3 Oct 2016 | OPTICS EXPRESS 23314

Optics EXPRESS

High throughput static channeled interference imaging spectropolarimeter based on a Savart polariscope

CHUNMIN ZHANG,[1,2] QIWEI LI,[1,3] TINGYU YAN,[1] TINGKUI MU,[1] AND YUTONG WEI[1]

[1]*Institute of Space Optics, School of Science, Xi'an Jiaotong University, Xi'an Shaanxi 710049, China*
[2]*zcm@mail.xjtu.edu.cn*
[3]*1003181800@qq.com*

Abstract: A high throughput static channeled interference imaging spectropolarimeter (CIISP) over 480–960nm spectral range is presented. The CIISP system includes two birefringent retarders and a Savart interferometer employing tempo-spatially mixed modulated mode with no internal moving parts, and offers a robust system and a high optical throughput to resist the instrument noise. The optical layout and operation of the CIISP sensor are presented in addition to the radiometric, spectral and improved polarimetric calibration techniques used with the system. The performance of the system is verified through laboratory tests, and the outdoor measurement demonstrates the sensor's ability for target identification, color measurement, and agriculture monitoring applications.

OCIS codes: (110.4234) Multispectral and hyperspectral imaging; (120.6200) Spectrometers and spectroscopic instrumentation; (260.5430) Polarization; (300.6300) Spectroscopy, Fourier transforms.

References and links

1. D. J. Diner, R. A. Chipman, N. Beaudry, B. Cairns, L. D. Food, S. A. Macenka, T. J. Cunningham, S. Seshadri, and C. Keller, "An integrated multiangle, multispectral, and polarimetric imaging concept for aerosol remote sensing from space," Proc. SPIE **5659**, 88–96 (2005).
2. F. Snik, T. Karalidi, and C. U. Keller, "Spectral modulation for full linear polarimetry," Appl. Opt. **48**(7), 1337–1346 (2009).
3. W. Groner, J. W. Winkelman, A. G. Harris, C. Ince, G. J. Bouma, K. Messmer, and R. G. Nadeau, "Orthogonal polarization spectral imaging: a new method for study of the microcirculation," Nat. Med. **5**(10), 1209–1212 (1999).
4. J. S. Tyo, D. L. Goldstein, D. B. Chenault, and J. A. Shaw, "Review of passive imaging polarimetry for remote sensing applications," Appl. Opt. **45**(22), 5453–5469 (2006).
5. R. S. Gurjar, V. Backman, L. T. Perelman, I. Georgakoudi, K. Badizadegan, I. Itzkan, R. R. Dasari, and M. S. Feld, "Imaging human epithelial properties with polarized light-scattering spectroscopy," Nat. Med. **7**(11), 1245–1248 (2001).
6. T. G. Moran and J. M. Davila, "Three-dimensional polarimetric imaging of coronal mass ejections," Science **305**(5680), 66–70 (2004).
7. J. Li, J. Zhu, and H. Wu, "Compact static Fourier transform imaging spectropolarimeter based on channeled polarimetry," Opt. Lett. **35**(22), 3784–3786 (2010).
8. K. Oka and T. Kato, "Spectroscopic polarimetry with a channeled spectrum," Opt. Lett. **24**(21), 1475–1477 (1999).
9. J. S. Tyo and T. S. Turner, Jr., "Variable-retardance, Fourier-transform imaging spectropolarimeters for visible spectrum remote sensing," Appl. Opt. **40**(9), 1450–1458 (2001).
10. S. Jones, F. Iannarilli, and P. Kebabian, "Realization of quantitative-grade fieldable snapshot imaging spectropolarimeter," Opt. Express **12**(26), 6559–6573 (2004).
11. R. W. Aumiller, C. Vandervlugt, E. L. Dereniak, R. Sampson, and R. W. McMillan, "Snapshot imaging spectropolarimetry in the visible and infrared," Proc. SPIE **6972**, 69720D (2008).
12. X. Meng, J. Li, D. Liu, and R. Zhu, "Fourier transform imaging spectropolarimeter using simultaneous polarization modulation," Opt. Lett. **38**(5), 778–780 (2013).
13. J. Craven-Jones, M. W. Kudenov, M. G. Stapelbroek, and E. L. Dereniak, "Infrared hyperspectral imaging polarimeter using birefringent prisms," Appl. Opt. **50**(8), 1170–1185 (2011).
14. M. W. Kudenov, N. A. Hagen, E. L. Dereniak, and G. R. Gerhart, "Fourier transform channeled spectropolarimetry in the MWIR," Opt. Express **15**(20), 12792–12805 (2007).

#272234 http://dx.doi.org/10.1364/OE.24.023314
Journal © 2016 Received 25 Jul 2016; revised 18 Sep 2016; accepted 19 Sep 2016; published 28 Sep 2016

Optics EXPRESS

15. J. Li, B. Gao, C. Qi, J. Zhu, and X. Hou, "Tests of a compact static Fourier-transform imaging spectropolarimeter," Opt. Express **22**(11), 13014–13021 (2014).
16. C. M. Zhang, L. B. Xiang, B. C. Zhao, and X. J. Yuan, "A static polarization imaging spectrometer based on a Savart polariscope," Opt. Commun. **203**(1–2), 21–26 (2002).
17. C. M. Zhang, X. Yan, and B. C. Zhao, "A novel model for obtaining interferogram and spectrum based on the temporarily and spatially mixed modulated polarization interference imaging spectrometer," Opt. Commun. **281**(8), 2050–2056 (2008).
18. X. Jian, C. Zhang, L. Zhang, and B. Zhao, "The data processing of the temporarily and spatially mixed modulated polarization interference imaging spectrometer," Opt. Express **18**(6), 5674–5680 (2010).
19. N. Hagen, E. L. Dereniak, and D. T. Sass, "Visible snapshot imaging spectro-polaimeter," Proc. SPIE **5888**, 588810 (2005).
20. H. W. Gao, C. M. Zhang, and B. C. Zhao, "Relative calibration for a polarization interference imaging spectrometer," Opt. Commun. **284**(12), 2747–2750 (2011).
21. A. Harvey and D. Fletcher-Holmes, "Birefringent Fourier-transform imaging spectrometer," Opt. Express **12**(22), 5368–5374 (2004).
22. S. Takahashi, J. S. Ahn, S. Asaka, and T. Kitagawa, "Multichannel Fourier transform spectroscopy using two-dimensional detection of the interferogram and its application to Raman spectroscopy," Appl. Spectrosc. **47**(7), 863–868 (1993).
23. M. W. Kudenov and E. L. Dereniak, "Compact real-time birefringent imaging spectrometer," Opt. Express **20**(16), 17973–17986 (2012).
24. A. Taniguchi, K. Oka, H. Okabe, and M. Hayakawa, "Stabilization of a channeled spectropolarimeter by self-calibration," Opt. Lett. **31**(22), 3279–3281 (2006).
25. K. Itoh, "Analysis of the phase unwrapping algorithm," Appl. Opt. **21**(14), 2470 (1982).
26. J. M. Craven, M. W. Kudenov, and E. L. Dereniak, "False signature reduction in infrared channeled spectropolarimetry," Proc. SPIE **7419**, 741909 (2009).
27. X. Meng, J. Li, H. Song, and R. Zhu, "Full-Stokes Fourier-transform imaging spectropolarimeter using a time-division polarization modulator," Appl. Opt. **53**(24), 5275–5282 (2014).

1. Introduction

An imaging spectropolarimeter (ISP) is capable of simultaneously measuring the three-dimensional spatial and spectral data cube for each of the Stokes parameters, S_0, S_1, S_2 and S_3. These four parameters constitute the Stokes vector $\vec{S}$ to specify the total intensity S_0, the ellipse of polarization, and the degree of polarization. The ISP device improves the ability of object detection with preferable accuracy, and has been recognized as a powerful tool in many fields, such as remote sensing, environmental monitoring, biomedical diagnosis, and other scientific areas [1–6]. However, in conventional ISP, rotating polarization elements, electrically controllable components, and micro-retarder or micro-polarizer arrays are typically required, which cause apparatuses generally suffer from vibration, electrical noise, and alignment difficulty [7].

Oka and Kato first described the channeled polarimetric technique in 1999 [8], by which all the Stokes parameters can be detected at once without movable polarization components or micro-components. Then channeled polarimetric technique is incorporated into different types of imaging spectrometers, such as Fourier transform imaging spectrometer (FTIS) [9], grating imaging spectrometer (GIS) [10], computed tomography imaging spectrometer (CTIS) [11] and so forth. Among these combinations, the channeled polarimetric technique has many unique benefits working with the FTIS, which maintains the throughput (Jacquinot) and multiplex (Fellgett) advantages [12]. Furthermore, the spectral carrier frequencies containing the Stokes parameter information can be acquired more directly using the channeled interferogram taken from the FTIS, which reducing the number of fast Fourier transforms (FFTs) required in postprocessing by 25% [13]. Kudenov et al. provided a non-imaging spectropolarimeter in the middle wave infrared (MWIR) using a commercial Michelson-interferometer-based FTS [14], which belongs to temporally modulated mode. Jie Li et al. proposed a compact static Fourier-transform imaging spectropolarimeter (FTISP) combined channeled polarimetry with a single Wollaston prism interferometer [15], while the spatially modulated mode brings a low optical throughput because of the slit used in optical layout. Jones et al. proposed an infrared hyperspectral imaging polarimeter (IHIP) based on a pair of moving Wollaston prisms employing tempo-spatially mixed modulated mode [13],

Optics EXPRESS

which has a high optical throughput and wide field of view. However, its internal mechanical moving parts restrict the temporal registration especially for remote sensing applications on moving platforms.

In this paper, we propose a high throughput static channeled interference imaging spectropolarimeter (CIISP) which combines the channeled polarimetric technique with a Savart interferomreter [16] for the first time. The device has no internal moving parts, electrically controllable or micro polarization components. It employs tempo-spatially mixed modulated mode using a field stop to replace the entrance slit [15], which brings the advantage of static state, high optical throughput, and easy alignment. Furthermore, the use of the SP leads to a compact system compared to Michelson or Sagnac interferometer [14]. The full wavelength-dependent state of polarization (SOP), spectral and spatial information of a scene can be acquired simultaneously. We describe the sensor configuration and theoretical model of the CIISP in Section 2. A systematic calibration of the sensor is implemented in Section 3, including relative radiometric, spectral, spectral responsivity, absolute radiometric and polarimetric calibration techniques. Section 4 presents the laboratory and outdoor data from the CIISP and discusses the results, while our conclusion is contained in Section 5.

2. Sensor configuration and theoretical model

2.1 Sensor configuration and data acquisition model

The optical layout of the CIISP based on a Savart polariscope (SP) is depicted in Fig. 1. Two birefringent crystal retarders, R_1 and R_2 with fast axes orientations at 0° and 45° relative to the horizontal, are installed behind the fore-optics. These are followed by a birefringent Fourier-transform imaging spectrometer which is composed of a linear polarizer P_1, a Savart lateral shearing splitter consisting of two identical uniaxial crystal plates with orthogonally oriented principal sections, an analyzer P_2, a reimaging lens L_3, and a charge-coupled device (CCD) placed on the back focal plane of L_3. The SP is rotated clockwise along z axis by 45° in order to maximize the fringes contrast. The optic axes of the two plates are oriented at 45° relative to the z axis and their projections on the x-y plane are oriented at ± 45° respectively relative to the x axis. The transmission axes of P_1 and P_2 are aligned with the fast axis of R_1.

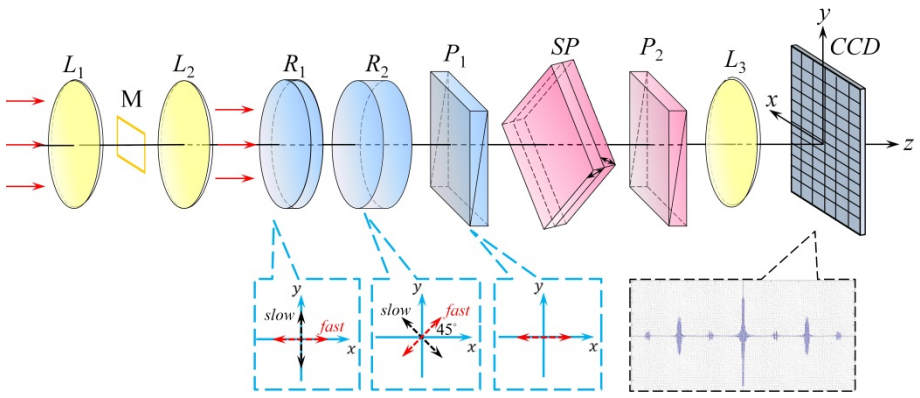

Fig. 1. Optical layout of the CIISP based on a Savart polariscope.

Light from the object is imaged on field stop M (located in intermediate image plane) by lens L_1 and then collimated by lens L_2. The parallel light passes through the two high-order birefringent retarders R_1, R_2, and a polarizer P_1, and becomes linearly polarized at 0° to the x axis. The 0° oriented polarized light is parallel laterally sheared by the Savart polariscope into a pair of equal-amplitude but orthogonally polarized components. After passing through P_2, the identical linearly polarized components are extracted and recombined onto the CCD camera by L_3. The imaging system superimposes the fringes with the scene which leads to an intensity modulated image. The optical path difference (OPD) is introduced by the shear of

Optics EXPRESS

SP which is the key component of the CIISP system. Note that the principal section of left plate of SP is oriented at 45° relative to the y-z plane, hence the fringe pattern is similar to that in the Young's double slit setup and is straight line that parallel to the x axis. Complete interferogram for the same object pixel can be collected by employing tempo-spatially mixed modulated mode (also called windowing mode) [17,18] as shown in Fig. 2.

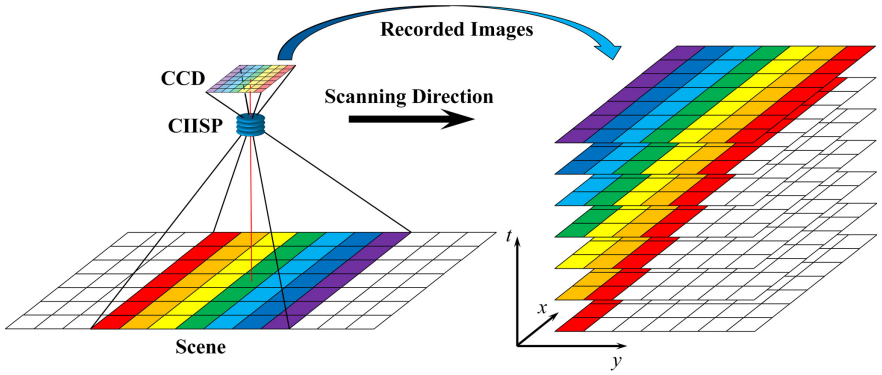

Fig. 2. Data acquisition model of the CIISP system.

The CIISP system can be equipped on aircraft or ground equipment such as translation stage and turntable. It moves over the whole area, every plot of the scene experiences the process that the incident angle changes from maximum, zero, finally to negative maximum. The CCD camera records a full two-dimensional image per frame, with successive frames associated with different OPD by scanning across a scene. Thereby, the whole interferogram data of a target have to be picked out from a series CCD images respectively and organize them regularly. The scan rate of the system is related to the acquisition time (t) of CCD camera. The camera uses a 512 × 512 element FPA with a pixel size of 18μm. To acquire the desired spectrum of scene in one column, it has to sample the complete OPD that 512 successive images need to be recorded, and take the scan time of 512t. The scan of a whole scene (512 × 512 plots) always takes less than 10s since the system has a high optical throughput, and leads to a short exposure time of CCD camera.

The CIISP system is relatively compact (~100 mm long, not including the imaging optics). A photograph of the core optics in CIISP sensor is shown in Fig. 3. The birefringent elements used in CIISP are made of two kinds of materials. The calcite prisms work as Glen-Taylor polarizers (extinction ratio ≥ 10^5) P_1, P_2, and the beam splitter SP. The quartz prisms are used for the two high-order retarders. The apex angle of all four prism wedges in P_1 and P_2 is nominally 39.7° with a ± 0.1° tolerance. The dimensions of SP which provides the maximum OPD of 61.44μm are $31mm \times 31mm \times 12mm$ with a fabrication tolerance of $\pm 0.1mm$ on each dimension. R_1 and R_2 are cylindrical 35mm diameter elements, with thicknesses of 1.9 and 3.8mm, respectively. Note that all birefringent elements are anti-reflection (AR) coated for wavenumber σ = 10416.67–20833.33cm^{-1} (wavelength λ = 480–960nm), providing >93% transmission through the birefringent interferometer. A commercial monochromatic Sarnoff CAM512 CCD camera is used to take the interferograms and images of the targets. The frame rate of the CCD camera can reach 250Hz to ensure speed of data collection.

Optics EXPRESS

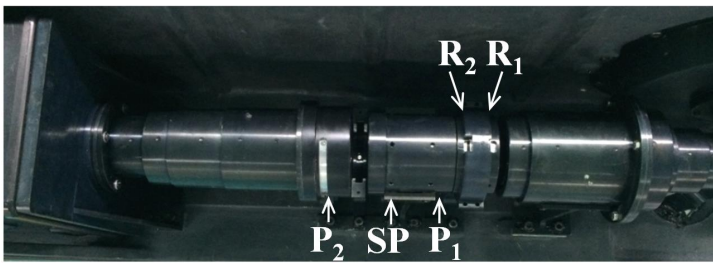

Fig. 3. Photograph of the core optics.

2.2 Theoretical model

With the use of Mueller calculus, the Stokes vector of the emergent light from the analyzer P_2 can be described as [8, 14]

$$\mathbf{S}_{\mathbf{out}} = \mathbf{M}_{\mathbf{P}_2}\mathbf{M}_{\mathbf{SP}}\mathbf{M}_{\mathbf{P}_1}\mathbf{M}_{\mathbf{R}_2}\mathbf{M}_{\mathbf{R}_1}\mathbf{S}_{\mathbf{in}} \tag{1}$$

where the quantities $\mathbf{M}_{\mathbf{R}_1}$, $\mathbf{M}_{\mathbf{R}_2}$, $\mathbf{M}_{\mathbf{P}_1}$, $\mathbf{M}_{\mathbf{SP}}$ and $\mathbf{M}_{\mathbf{P}_2}$ are the Muller matrices of the retarders R_1 and R_2, the polarizer, the SP and the analyzer, respectively. $\mathbf{S}_{\mathbf{in}}(\boldsymbol{\sigma}) = [S_0(\sigma)S_1(\sigma)S_2(\sigma)S_3(\sigma)]^T$ is the spectrally resolved Stokes vector of the incident light, where $S_0(\sigma)$ is the total intensity of the light, $S_1(\sigma)$ is the horizontal linearly polarized intensity minus the vertical linearly polarized intensity, $S_2(\sigma)$ is the 45° linearly polarized intensity minus the 135° linearly polarized intensity, and $S_3(\sigma)$ is the difference between the left and right circularly polarized intensities. The digital camera responds to radiation intensity instead of polarization state, so only the first parameter of $\mathbf{S}_{\mathbf{out}}$ can be measured. The fringe pattern intensity of a single object point can be expressed as [13]

$$\begin{aligned} I_{CCD}(z) \propto \int \frac{(1+\cos\varphi_Z(\sigma))}{4}[\, & S_0(\sigma) + S_1(\sigma)\cos(\varphi_2(\sigma)) \\ & + S_2(\sigma)\sin(\varphi_1(\sigma))\sin(\varphi_2(\sigma)) - S_3(\sigma)\sin(\varphi_1(\sigma))\cos(\varphi_2(\sigma))\,]\, d\sigma \end{aligned} \tag{2}$$

The phase term corresponding to the OPDs are given by

$$\varphi_Z(\sigma) = 2\pi\Delta z\sigma \tag{3}$$

$$\varphi_1(\sigma) = 2\pi L_1\sigma \tag{4}$$

$$\varphi_2(\sigma) = 2\pi L_2\sigma \tag{5}$$

where Δz is the OPD from the SP. $L_i = B(\sigma)d_i$, $(i = 1, 2)$ characterize the OPD introduced by R_1 and R_2, where $B(\sigma)$ is the birefringence of the birefringent crystal. d_1 and d_2 are the thicknesses of retarders, which are chosen to be $d_1 = d_2/2$ in presented system. Expanding Eq. (6) yields seven frequency channels that contain the polarimetric information

$$\begin{aligned} I_{CCD}(z) \propto \int \frac{(1+\cos\varphi_Z)}{2}[\, & S_0 + \frac{S_1}{2}e^{i\varphi_2} + \frac{S_1}{2}e^{-i\varphi_2} + \frac{S_2+iS_3}{4}e^{-i(\varphi_1-\varphi_2)} \\ & + \frac{S_2-iS_3}{4}e^{i(\varphi_1-\varphi_2)} + \frac{-S_2+iS_3}{4}e^{i(\varphi_1+\varphi_2)} + \frac{-S_2-iS_3}{4}e^{-i(\varphi_1+\varphi_2)}\,]\, d\sigma \end{aligned} \tag{6}$$

From Eq. (6), there are seven distinct channels which contain the data related to the input Stokes parameters. These channels can be seen from a real interferogram collected with the CIISP shown in Fig. 4, where a 22.5° linear incident polarization state and a broad band

Optics EXPRESS

source were used to produce the interferogram. It can be shown that the seven channels, C_i, $(i = 0, \pm1, \pm2, \pm3)$, are centered at $OPD = 0, \pm L_2, \pm(L_1 - L_2)$ and $\pm(L_1 + L_2)$, respectively.

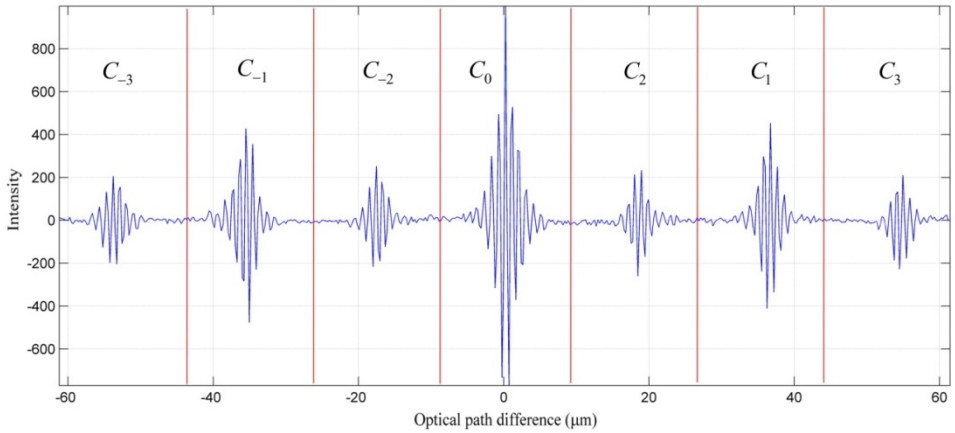

Fig. 4. Interferogram of the CIISP for a 22.5° linear incident polarization state. The 7 channels in interferogram are separated in OPD space by the retardations φ_1 and φ_2. Spacing between each channel is for a 2:1 thickness ratio ($d_2 : d_1$) using our setup.

Filtering channels C_0, C_{-1} and C_{-2} at each pixels and followed by a fast Fourier transform (FFT), enable demodulation of the spectrally-dependent Stokes parameters:

$$\Im\{C_0\} = \frac{1}{2} S_0(\sigma) \tag{7}$$

$$\Im\{C_{-1}\} = \frac{1}{4} |S_1(\sigma)| \exp\{i[\varphi_2(\sigma) + \arg\{S_1(\sigma)\}]\} \tag{8}$$

$$\Im\{C_{-2}\} = \frac{1}{8} |S_{23}(\sigma)| \exp\{i[\varphi_2(\sigma) - \varphi_1(\sigma) + \arg\{S_{23}(\sigma)\}]\} \tag{9}$$

where $S_{23}(\sigma) = S_2(\sigma) + iS_3(\sigma)$ and arg stands for the operator to take the argument. In Eq. (7)-(9), only S_0 parameter can be demodulated directly, while S_1, S_2 and S_3 parameters are still modulated by φ_1 and φ_2. The phase factors in C_{-1} and C_{-2} can be calibrated out to reconstruct the full Stokes parameters detailed in Section 3.4. The data reconstructed by CIISP system can be viewed as a four-dimensional spectropolarimetric hypercube as presented in Fig. 5. The dimensions of this volume are given by two spatial dimensions (x,y), a wavenumber dimension (σ), and an index dimension (j) corresponding to the index of the Stokes vector components [19]. Note that the Stokes vector index has only four possible values (j = 0, 1, 2, 3), whereas the x, y, and σ dimensions will each be segmented into a greater number of intervals.

Optics EXPRESS

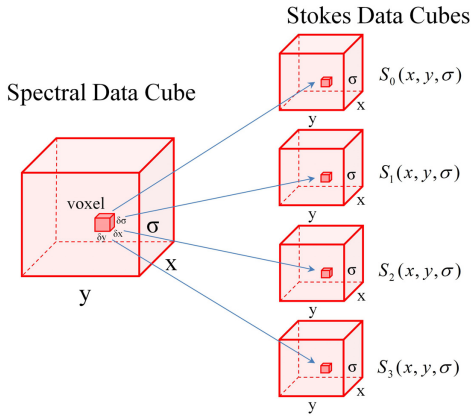

Fig. 5. The spectropolarimetric hypercube acquired by the CIISP system.

3. Sensor calibration and performance characterization

3.1 Relative radiometric calibration

The non-uniformity response of CCD camera will lead to striping and banding in the image [20]. In order to reconstruct the complete Stokes parameters from the scene without including background effects, detector offsets must be accounted for via a relative radiometric calibration of the sensor. However, the instrument has been installed completely that the CCD can't be calibrated alone, and the interferogram fringes in focal plane array will affect the uniformity of the detector. Fortunately, the fringe pattern is straight line which is parallel to the column pixels, hence the calibration was done by pixels in each column which ideally have the same brightness.

The digital number (DN) of CCD dark current at the (i, j) pixel, $D^t_{i,j}$, was recorded with exposure time of 5ms to 95ms in equal increments of 10ms first. Then a uniform light source integrating sphere (Labsphere XTH2000) was used to generate unpolarized polychromatic lights, which was placed sufficiently close to the system such as to fill the entrance pupil. The light intensity is adjustable to offer various radiance values (L) covering the dynamic range of the CCD with each exposure time. The interferogram images recorded by the instrument should be subtracted by the dark current of CCD given as $N^t_{i,j}(L) = N^t_{0_{i,j}}(L) - D^t_{i,j}$, where $N^t_{0_{i,j}}(L)$ is the original DN of the (i, j) pixel with exposure time of t. The calibration coefficient $K^t_{i,j}(L)$ is defined as $K^t_{i,j}(L) = N_{mean_j}{}^t(L) / N^t_{i,j}(L)$, where $N_{mean_j}{}^t(L)$ is the average DN of the jth column. The least square fit was employed to describe the relationship between $K^t_{i,j}$ and $N^t_{i,j}$, here the linear fitting was selected and given in Eq. (10) since the pixels have good linearity.

$$K^t_{i,j}(L) = R^t_{i,j} N^t_{i,j}(L) + O^t_{i,j} \tag{10}$$

In Eq. (10), $R^t_{i,j}$ and $O^t_{i,j}$ are the multinomial coefficients. Each pixel of input interferogram images are subtracted by the dark current, and multiplied by $K^t_{i,j}(L)$ to constitute the output interferogram images as can be seen in Fig. 6. It shows that the non-uniformity of CCD image caused by manufacturing defects and vignetting artifacts of the complete instrument has been well improved after relative radiometric calibration. Figure 7 shows the DN values of an arbitrarily selected row and column pixels from the two images. In Fig. 7(a), the DN values in the original data are within a large range from 1697 to 1983, reduced to 1837–1875 after

Optics EXPRESS

calibration, and the data curve tends to be a straight line without burr. Figure 7(b) shows that the interferogram becomes more symmetrical after calibration. The data of interferogram with high signal noise ratio located on both sides of zero OPD point are well preserved, and the step changes of DN values caused by CCD light-sensitive component junctures are also been well corrected.

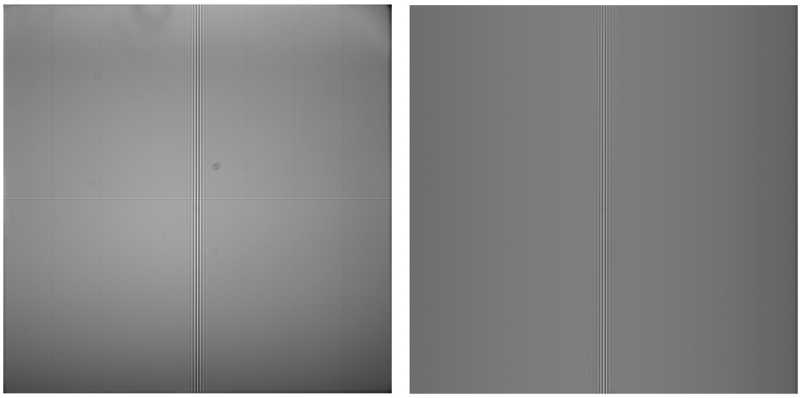

Fig. 6. (Left) Raw interferogram image of an unpolarized polychromatic light with 5ms exposure time. (Right) Image data after relative radiometric calibration.

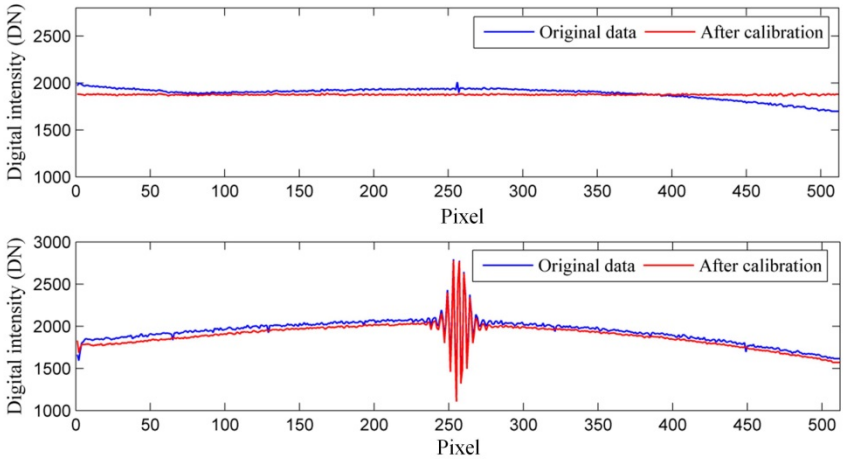

Fig. 7. DN value of pixels in column 200 (the upper) and row 200 (the lower) from the two images.

3.2 Spectral calibration

Spectral calibration of the CIISP system based on Savart polariscope involves compensating for the dispersion of the birefringent crystal [21], and first requires that the spectral wavenumber axis, $\vec{\sigma} = [-\sigma_{\max}, -\sigma_{\max} + \Delta\sigma, ..., \sigma_{\max} - \Delta\sigma, \sigma_{\max}]$, be calculated assuming that the OPD is achromatic. The $\sigma_{\max}$ is the maximum spectral frequency that is reconstructed, which can be acquired by using the Nyquist-Shannon sampling theorem, $\sigma_{\max} \le 1/2\Delta\delta$, where $\Delta\delta$ is the change in OPD between frames of data. However, the SP will introduce non-ignorable quadratic OPD [22] at a large incident angle (>3°) which makes the total OPD changed approximately linearly with rows when the maximum incident angle of the SP is designed with 3.65°. Figure 8(a) depicts the fringe pattern of the channeled interferogram captured by CIISP, and the fringes in large-OPD area are not vertical because the absolute

Optics EXPRESS

value of maximum OPD is increased with rows. Therefore, $\sigma_{\max}$ is no longer a constant but varied with rows.

The spectral calibration can be performed using a monochromatic light as the calibration source with a known wavenumber σ_{ref}. The laser light with wavelength of 650nm ($\sigma_{ref} = 15385 cm^{-1}$) was selected since it is in visible band and will not be affected by spectral aliasing if slight undersampling of the interferogram occurs. Figure 8(b) depicts the calculated distribution of total $OPD_{ref}(x, y)$ in each pixel at σ_{ref} based on paraxial approximation

$$OPD_{ref}(x,y) = \sqrt{2}t\frac{n_o^2 - n_e^2}{n_o^2 + n_e^2}\frac{x}{f} + \frac{t}{\sqrt{2}}\frac{n_o}{n_e}\frac{n_o^2 - n_e^2}{(n_o^2 + n_e^2)^{3/2}}\frac{2xy}{f^2} \tag{11}$$

where x, y are the horizontal and the vertical distance between the selected pixel and the central point of the focal plane array, respectively, t is the thickness of a single plate in the SP, n_o and n_e are the ordinary and extraordinary refractive indices of calcite material at σ_{ref}, f is the focal length of the reimaging lens L_3. It has been shown that the maximum OPD is increased linearly with rows, which coincides with the experimental result analyzed above. Therefore, the discrete linear wavenumber axis of each row, $\bar{\sigma}_{1,i}$, can be acquired according to the achromatic model in Eq. (11), which requires adjustment to remove the birefringence dispersion's influence.

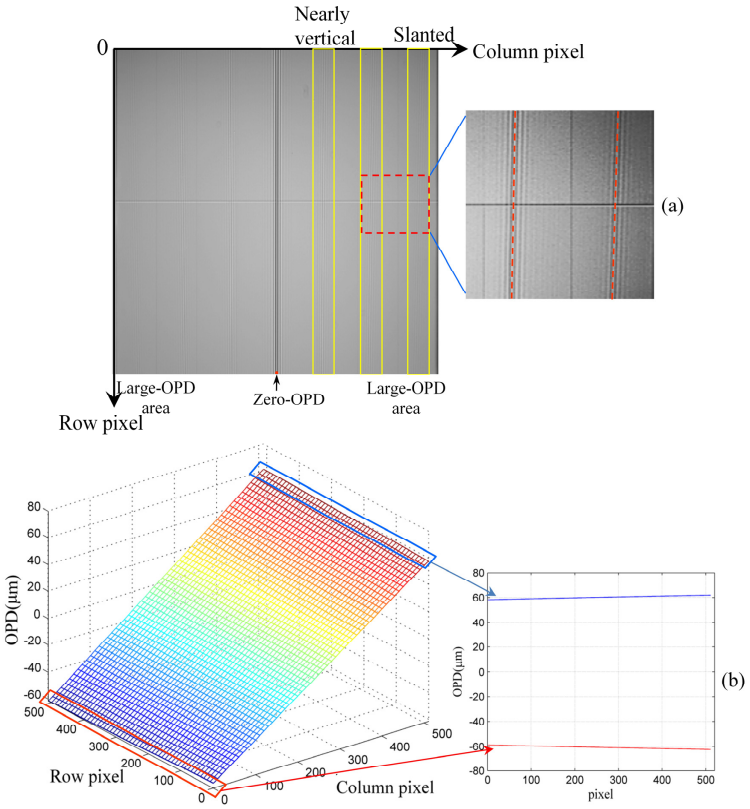

Fig. 8. (a) Interference fringes are slanted to the right in large-OPD area in the right part of the scene. (b) The distribution of total OPD in each pixel calculated at the calibration laser's wavenumber.

Optics EXPRESS

A birefringent prism's OPD can be expressed by a multiplication between an achromatic OPD and a birefringence ratio as [23]

$$OPD_i = OPD_{ref,i}\frac{B(\bar{\sigma}_{1,i})}{B(\sigma_{ref})} \tag{12}$$

where $OPD_{ref,i}$ is the optical path difference calculated at σ_{ref} in each row. $B(\bar{\sigma}_{1,i})$ can be acquired using the Sellmeier equation which enables the birefringence to be modeled as a function of wavenumber. After Fourier transformation of the interferogram, the birefringence ratio remains as a multiplicative factor to the wavenumber $\bar{\sigma}_{1,i}$. Once $B(\bar{\sigma}_{1,i})$ is calculated, $\bar{\sigma}_{1,i}$ is weighted by the birefringence ratio's inverse to correct for the dispersion errors:

$$\bar{\sigma}_{offset,i} = \bar{\sigma}_{1,i}\frac{B(\sigma_{ref})}{B(\bar{\sigma}_{1,i})} \tag{13}$$

where $\bar{\sigma}_{offset,i}$ is the dispersion-compensated, resampled nonlinear wavenumber axis. Note that the multiplication in Eq. (13) is performed in a way of element-by-element .

The feasibility of spectral calibration is demonstrated by using both monochromatic and polychromatic lights. The results are shown in Fig. 9. The reconstructed wavelengths of four laser lights centered at 543.5, 594.1, 612, and 632.8nm, respectively, coincide exactly with the input wavelengths of the selected rows, and the average error is less than 1.8nm. The polychromatic light results are also satisfactory. It can be seen that the reconstructed wavelengths of spectral characteristic peaks of Xenon lamp coincide with the values measured by a commercial ASD FieldSpec4 spectral radiation meter (SRM).

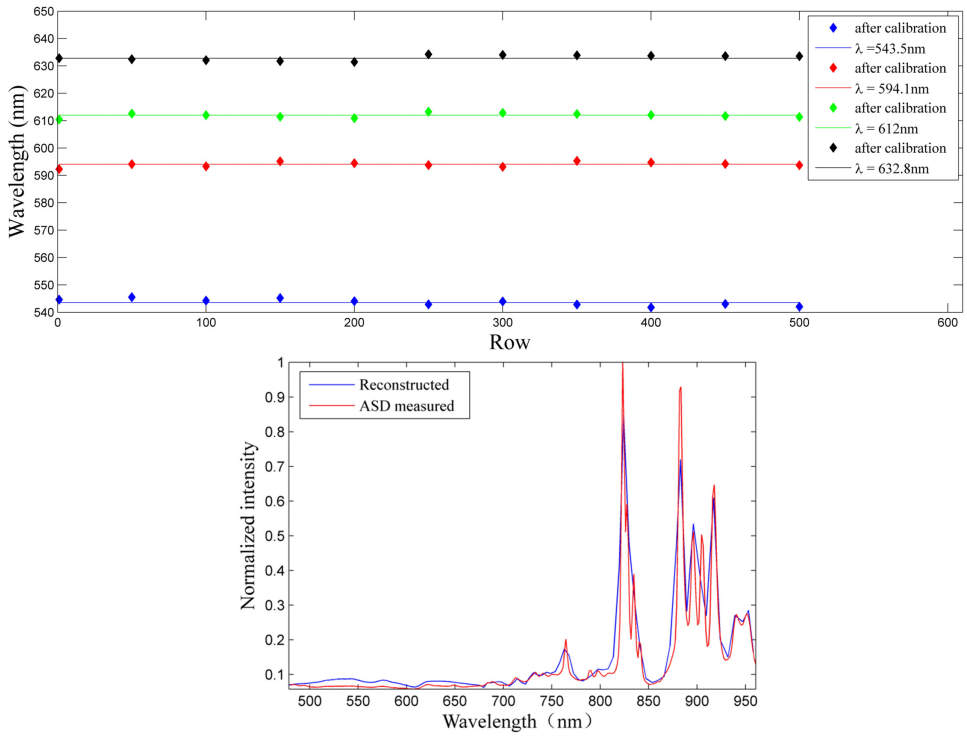

Fig. 9. Spectral calibration results of four monochromatic laser lights in short wavelength band with selected rows (the upper), and the polychromatic xenon light (the lower).

Optics EXPRESS

3.3 Spectral responsivity calibration and absolute radiometric calibration

The transmittance of optical element in the detecting spectral range and the spectral responsivity of CCD camera vary with wavelength. The spectral responsivity of the complete instrument should be determined through spectral responsivity calibration. It was performed using a monochromator as the light source to generate the monochromatic light ranging from 480nm to 960nm in equal increments of 5nm. The monochromatic lights were conducted to integrating sphere via fiber to generate unpolarized uniform lights, and the probe of the SRM was placed next to the device recording the radiance (L) with the instrument simultaneously. The DN value of each pixel across the FPA was collected and averaged over 20 sequential measurements. The normalized spectral responsivity (NSR) of the instrument can be acquired from the DN value and measured radiance shown in Fig. 10. It can be seen that the NSR is less than 0.5 in 480–520nm and 910–960nm. Using high-order polynomial curve fitting to smooth the measurement data, the jitter of the reconstructed spectrum can be reduced.

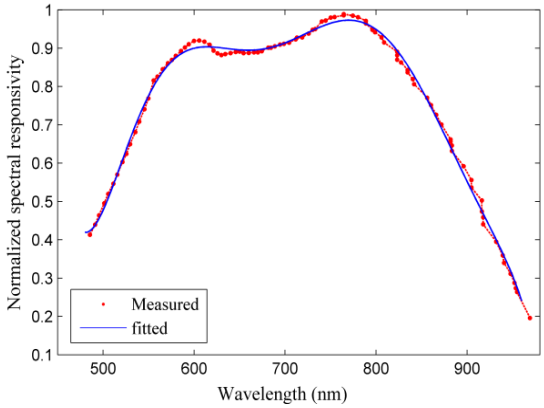

Fig. 10. Normalized spectral responsivity of the instrument.

Absolute radiometric calibration was also introduced to establish the functional relation between reconstructed spectrum and measured spectral radiance. A series of unpolarized polychromatic lights with different intensities were recorded by instrument and SRM simultaneously as mentioned in Section 3.1. The reconstructed spectral data M_k in band λ_k, is a dimensionless number. The relationship between M_k and the measured spectral radiance by SRM can be given as

$$L_k = E_k M_k + F_k \tag{14}$$

where E_k and F_k are the linear fitting coefficients and determined for each band. Note that the M_k values have been processed via spectral calibration and spectral responsivity calibration. Figure 11(a) depicts the linear fitting result of band σ = 13862cm^{-1} (λ = 721.4nm), which was produced using all fifteen data points. The fitting line coincides perfectly with the sample data, while the last point deviating from the line can be ignored since the CCD camera was overexposed. Figure 11(b) demonstrates the comparison between SRM measured spectrum and the reconstructed spectrum of a halogen tungsten lamp after absolute radiometric calibration. The red and blue curves almost overlap over each other in the middle of the detecting band, while the errors increased at the edges of the spectral band correspond to the low NSR of the instrument, and also have contributions from the weak light intensity in short-wavelength band.

Optics EXPRESS

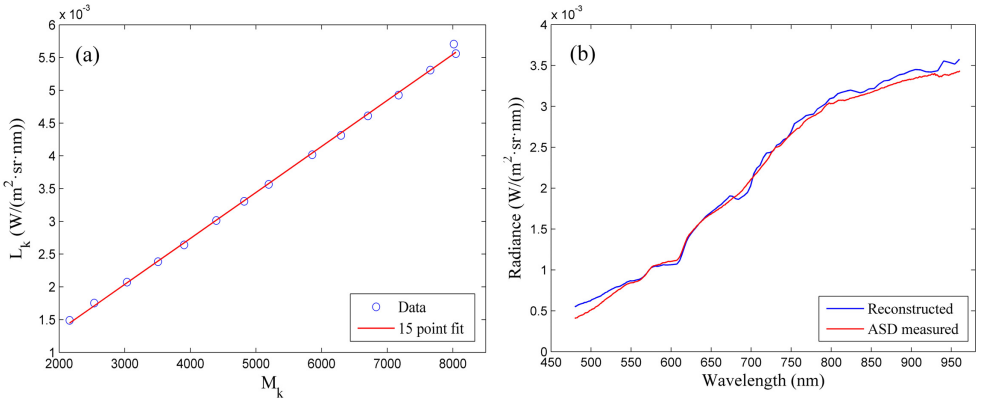

Fig. 11. (a) Effect of the linear fitting with all 15 points. (b) Spectrum from the CIISP sensor (blue line) and standard spectral radiation meter (red line). The spectral resolution of the CIISP system is approximately 81.3cm^{-1} (1.9nm) for the cutoff wavelength of 480nm.

3.4 Polarimetric calibration

In order to reconstruct the unknown Stokes parameters by eliminating the modulation with carrier frequencies' phase factors, φ_1 and φ_2, a calibration routine must be implemented. There are two kinds of mainstream techniques for performing this kind of polarimetric calibration. Reference beam calibration technique involves measuring a known reference state of polarization (SOP) to correct the modulating phase factors [13]. The other calibration method using self-calibration technique is appropriate for retarders in the presence of thermal fluctuations [24], and no reference beam is needed. The first method is preferable for our sensor since the retarders are not setup appropriately to make the necessary assumption that both retarders experience identical environmental changes.

In reference beam calibration technique, the phase factors φ_2 found in channel $C_{-1,\text{sample}}$ is divided by the "reference data" given as

$$S_{1,sample}(\sigma) = \cos 2\theta \,\mathrm{Re}\left|\frac{\Im(C_{-1,sample})}{\Im(C_{-1,reference,\theta})/S_{0,reference,\theta}}\right| \tag{15}$$

where θ is the angle of linearly polarized reference beam. In this form of calibration, φ_2 is eliminated since the phase factor is only the function of wavenumber when the thickness and material of R_2 are determined, and thus it is independent from the SOP of the incident light. However, the amplitude ratio, $\Im(C_{-1,reference,\theta})/S_{0,reference,\theta}$, is not always be offset by the theoretical value $\cos 2\theta$ because of the amplitude error in $C_{-1,reference,\theta}$ channel introduced by the instrument. Note that the amplitude error exists in $C_{-2,reference,\theta}$ channel as well, and will lead to an inaccurate reconstructed result of each Stokes parameter.

To solve this problem, we calculate the phase factor, φ_1 and φ_2, directly from the 'reference data' with known SOP. 22.5° linearly polarized light is selected as the reference beam since it can provide large amplitude modulations in both of the $C_{-1,reference,\theta}$ and $C_{-2,reference,\theta}$ channels. Taking demodulation of φ_2 as an illustration, the total phase including $\arg\{S_1(\sigma)\}$ and the retardation φ_2 can be calculated as

$$\varphi_{2all} = \arctan\left\{\frac{\mathrm{Im}[\Im\{C_{-1,reference,\theta}\}]}{\mathrm{Re}[\Im\{C_{-1,reference,\theta}\}]}\right\} \tag{16}$$

Optics EXPRESS

The retardation φ_2 can be acquired using general phase unwrapping algorithm [25] from $\varphi_{2all}(\sigma)$ with a known $\arg\{S_1(\sigma)\}$ since the absolute value of phase differences between neighbouring pixels is less than π with $|\Delta\varphi_2(\sigma)| = 0.528\pi$. In this form of calculation, the amplitude error mentioned above does not exist since $\varphi_{2all}(\sigma)$ is acquired only using the $C_{-1,reference,\theta}$ channel where $S_{0,reference,\theta}$ is not introduced, and the amplitude of $S_{1,reference,\theta}$ is cancelled out in Eq. (16). The same process can be applied to $C_{-2,reference,\theta}$ channel with phase difference of $|\Delta[\varphi_2(\sigma)-\varphi_1(\sigma)]| = 0.264\pi$, which is easier to meet condition of phase unwrapping algorithm. Therefore, $S_{1,sample}$ and $S_{23,sample}$ can be obtained using

$$S_{1,sample}(\sigma) = \Im\{C_{-1,sample}\}\cdot\exp[-i\varphi_2(\sigma)] \tag{17}$$

$$S_{23,sample}(\sigma) = \Im\{C_{-2,sample}\}\cdot\exp\{i[\varphi_1(\sigma)-\varphi_2(\sigma)]\} \tag{18}$$

Using the improved model, the experimental data are available for the generated SOP at various rotation angles of the generating polarizer from 0° to 180°. The reconstructed results of the normalized Stokes parameters obtained as a function of polarizer rotation angle and wavenumber, portrayed in contour plots, can be seen below in Fig. 12.

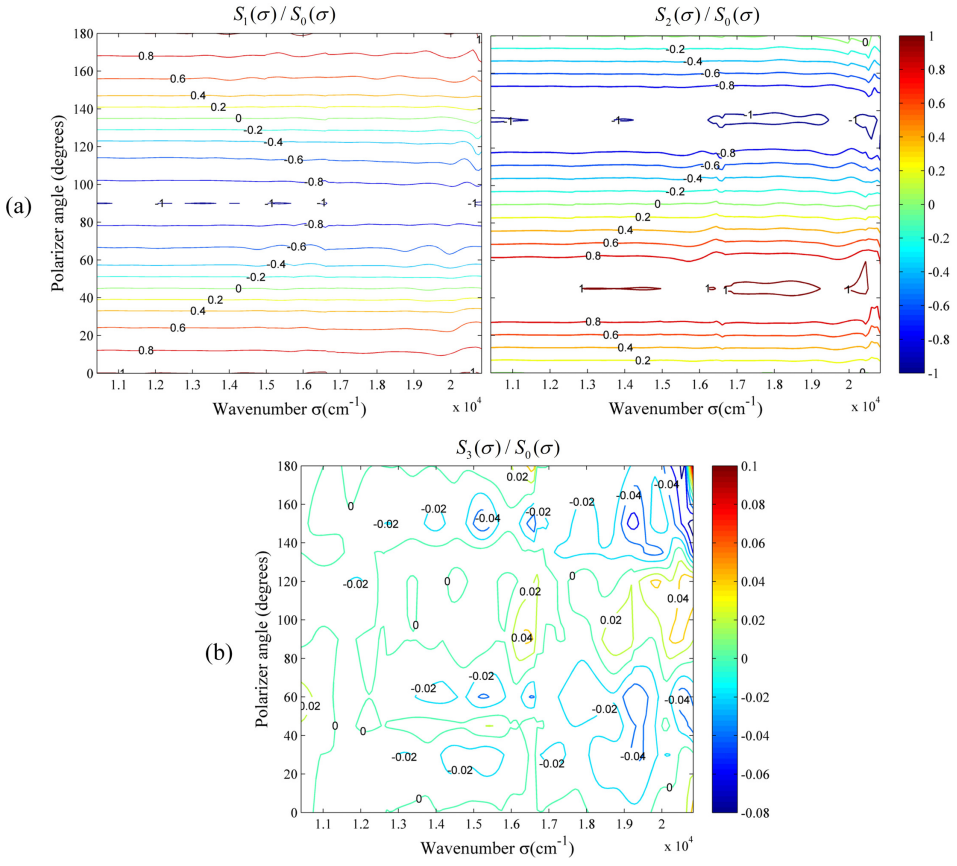

Fig. 12. Contour plots of the reconstructed results for the normalized Stokes parameters S_1, S_2 (a), and S_3 (b) using the improved method.

Note that the contours of the data in Fig. 12(a) should ideally consist of straight lines for S_1 and S_2. The values of the curves are smooth and accurate in $\sigma \le 1.9\times10^4 cm^{-1}$ ($\lambda \ge$

Optics EXPRESS

526.3nm), while the error is increased at the edges of the band due to the low intensity of the halogen tungsten lamp in short wavelength band shown in Fig. 11(b). Figure 12(b) can be seen as the error distribution in the reconstruction of S_3. The RMS error calculations were performed over the 10416.67–20833.33cm^{-1} (λ = 480–960nm) spectral band relative to the known input states, the results show that the average RMS error in each normalized Stokes parameter is given by $\varepsilon_{S1}^{rms} = 1.96\%$, $\varepsilon_{S2}^{rms} = 3.23\%$, $\varepsilon_{S3}^{rms} = 2.85\%$. These results can be compared to the RMS errors of $\varepsilon_{S1}^{rms} = 2.75\%$, $\varepsilon_{S2}^{rms} = 4.42\%$, $\varepsilon_{S3}^{rms} = 3.78\%$ given by the reference beam calibration technique for the same bandpass in the reconstructed Stokes parameters. Note that the two calibration methods used the same interferogram image of 22.5° linear reference beam to make them in the same condition.

4. Experiment results

4.1 Laboratory tests

Two experiments were performed to test the performance of the CIISP. The target of the first experiment was illuminated by a LED lamp with 0° linear polarization state. The light intensity outside 480–700nm is too small, as it is restricted by the LED spectral character. Therefore, a halogen lamp was used as the light source in the second experiment, and formed a complementary to provide high quality light in 700–960nm band, and the SOP of target is also changed to 45° linear. The experimental setup is shown in Fig. 13. The polychromatic light was conducted to integrating sphere to generate uniform and unpolarized light to illuminate the target. The flower and plane pictures were printed on translucent parchment paper as the targets, which were located in focal plane of the collimator to generate parallel beam detected by the sensor. A metal wire grid linear polarizer was located on the back of part scene to create a controlled SOP. The CIISP system was mounted on a uniaxial turntable with high angular resolution and high rate stability to scan across the scene. The exposure time of CCD camera was set to 5ms, and the angular velocity of turntable was 0.046°/s to meet the sampling requirement of interferogram. It took about 5.2s to scan the whole scene.

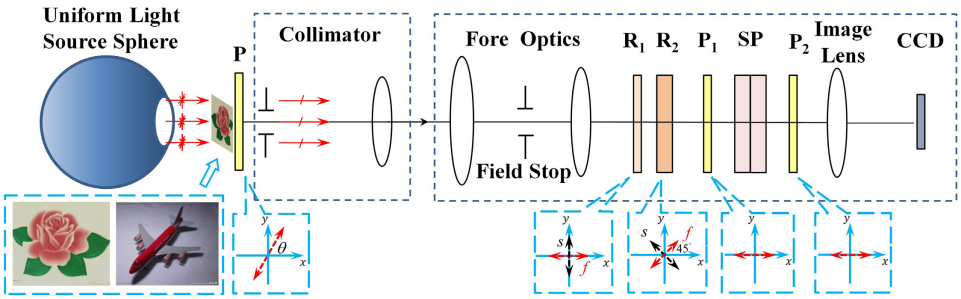

Fig. 13. Experiment setup for laboratory testing of the CIISP. The uniaxial turntable is not shown.

The interferometric images with 0° and 45° linear polarization states were captured. Figure 14 shows the two channeled interferograms after background elimination. It can be seen that the intensity of $C_{\pm 2}$, $C_{\pm 3}$ channels in Fig. 14(a), and $C_{\pm 1}$ channels in Fig. 14(b) are almost zero, in agreement with the corresponding normalized Stokes parameters [1 1 0 0] and [1 0 1 0], respectively.

Optics EXPRESS

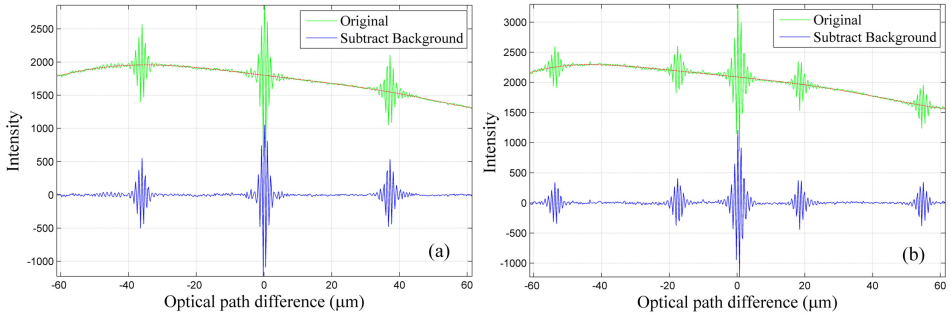

Fig. 14. Recorded channeled Interferograms for 0° (a) and 45° (b) linear polarization states after scanning and data preprocessing. The background (red line) was removed using the least squares method.

The results of the rose picture with 0° linear polarization state are discussed first. The spectropolarimetric information of the scene is calculated via Eq. (7)–(9). After data reconstruction, we obtained the spectropolarimetric images of the scene. Figure 15 shows four normalized recovered spectral images with their center wavelengths around 520, 570, 620, and 670nm, respectively. The spectral signatures of peach petal and green leaf can be clearly distinguished. The gradual decrease in intensity in the top edge of the FOV and the black area in four corners of the images are produced by obstruction of the collimator with a small field of view.

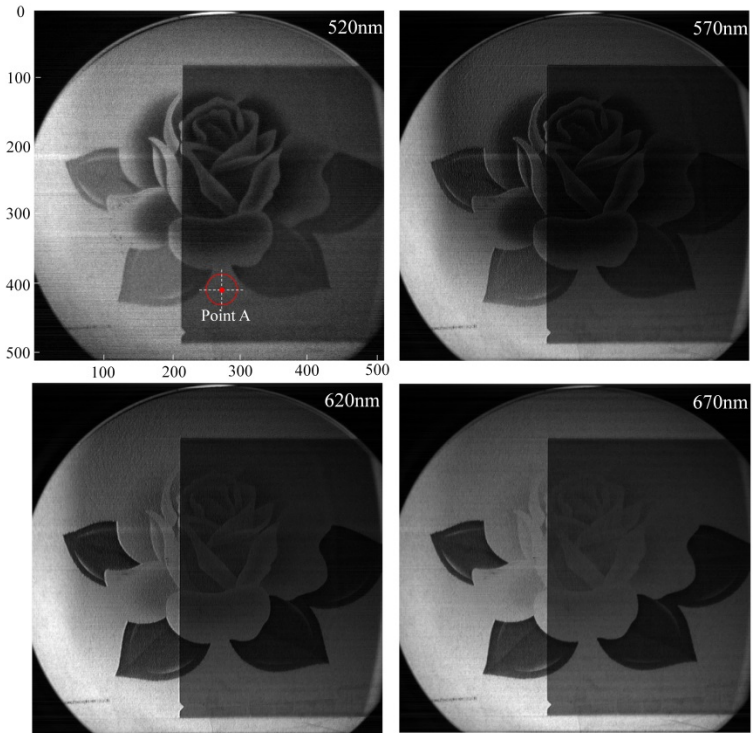

Fig. 15. Four spectral images of the scene at 520, 570, 620, and 670nm, respectively.

Figure 16 shows the spectral curve and normalized Stokes parameter of point A (row, column) = (410, 275), whose approximate location is marked in the first image of Fig. 15. The curves of the normalized Stokes parameters demonstrate good agreement with the theoretical values in $\sigma > 1.4\times10^{4}\,cm^{-1}$ (λ<714nm) band, while in $\sigma \le 1.4\times10^{4}\,cm^{-1}$ band the

Optics EXPRESS

curves tend to be fluctuant and deviate from the theoretical values mainly because of the measurement error due to the too weak light intensity, and the low spectral responsivity in this band. The normalized Stokes parameter images around 620nm ($\sigma = 16129 cm^{-1}$) are shown in Fig. 17. The region where a linear polarizer is located contains obviously linearly polarized information in S_1 image, while the intensity of the region in S_2 and S_3 images turns to be almost zero because of the characteristic of the 0° linear polarization state.

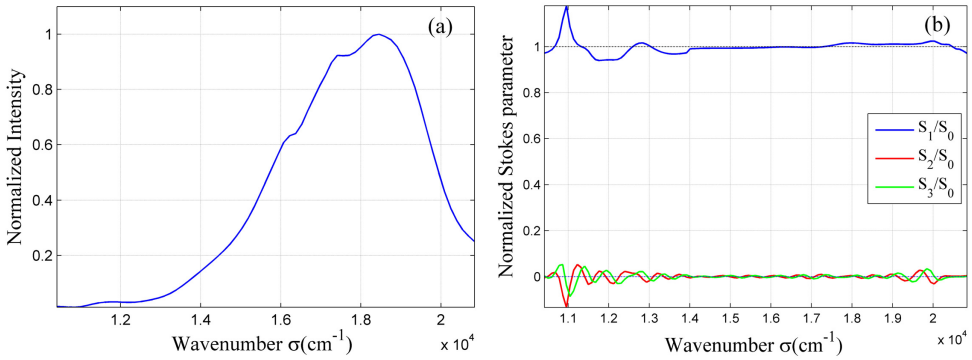

Fig. 16. (a) Spectrum of point A (row, column) = (410, 275) with Stokes parameter S_0. (b) Normalized Stokes parameters.

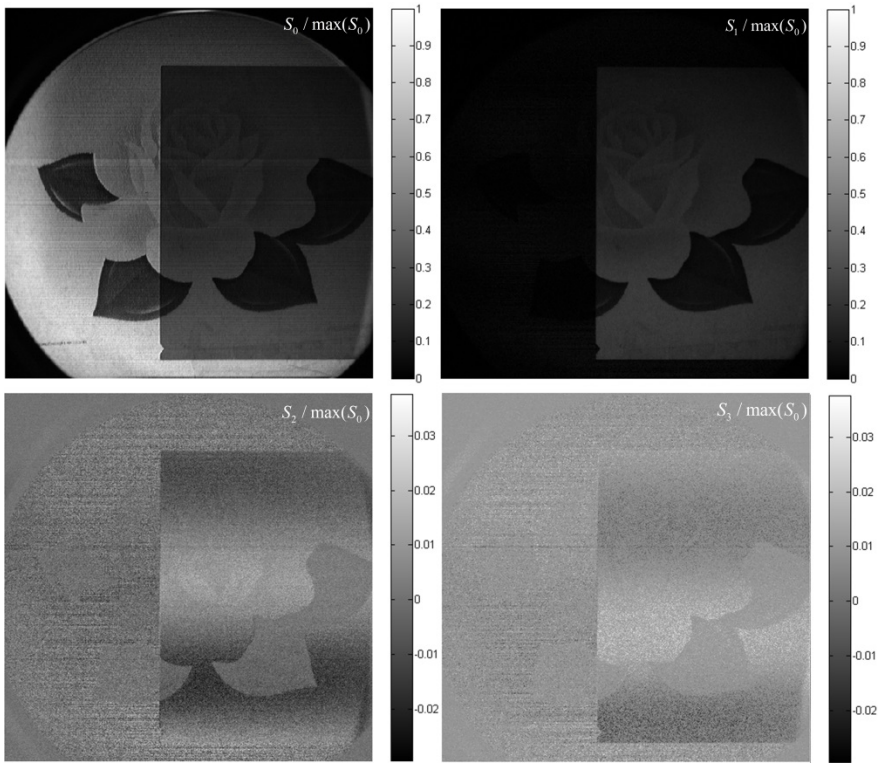

Fig. 17. Normalized Stokes parameter images at 620nm.

To verify the abilities for polarization detection in $\sigma \le 1.4\times10^4 cm^{-1}$ band, an additional experiment was presented using halogen lamp whose spectral characteristics are similar to Fig. 11(b) to provide high quality light in this band. The polarizer was rotated to generate 45° linear polarization state. The normalized recovered spectral image around σ = 11338cm^{-1} (λ =

Optics EXPRESS

882nm) is shown in Fig. 18(a). Figure 18(b) depicts the normalized Stokes parameters of point B (row, column) = (209, 350) in σ = 10417–14286cm^{-1} (λ = 700–960nm). Compared with the theoretical values, the experimental results are shown to yield accuracy better than 3.5% over the band. The residual error can likely be attributed to the retarders' misalignment and cross talk of the channeled interferogram [26,27]. The band integrated data of degree of polarization (DoP) spatial images are depicted in Fig. 19. The DoP is calculated from S_0, S_1, S_2 and S_3 using [13]

$$DoP(\sigma) = \frac{\sqrt{S_1(\sigma)^2 + S_2(\sigma)^2 + S_3(\sigma)^2}}{S_0(\sigma)} \tag{19}$$

The DoP data within the region where the polarizer is located are much higher than the uncovered parchment paper and the values are close to 1.

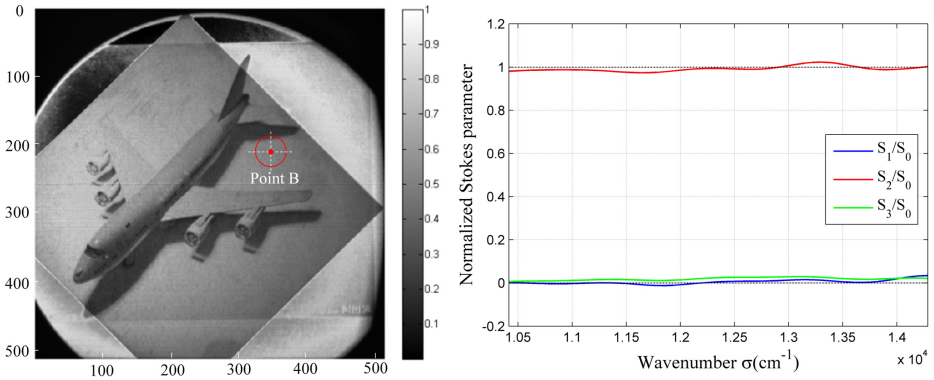

Fig. 18. (a) Spectral images of the scene at 882nm. (b) Normalized Stokes parameters of point B (row, column) = (209, 350).

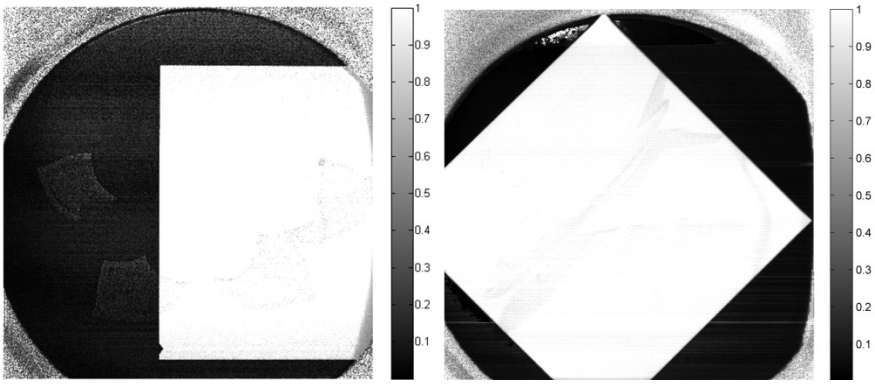

Fig. 19. Band integrated DoP spatial images of 0° (left) and 45° (right) linear polarization states.

4.2 Outdoor test

The system was located to a roof on the Xi'an Jiaotong University campus and was used to collect interferometric data of the scene depicted in Fig. 20(a), as imaged by the system. The scene was composed primarily of a building with glass windows in front of the forest at a distance of nearly 5km. The data were acquired with an integration time of 1/100th of a second in the late afternoon on a clear day. The normalized S_0 spectra of two selected pixels from the scene are depicted in Fig. 20(b). The two spectra illustrate the distinctions between

Optics EXPRESS

the spectra recovered from the building wall and the plant of the image. Note that the natural leaves' spectrum increases past 1.41cm^{-1} (710nm) due to chlorophyll, and the near-infrared light is strongly reflected while the visible-band light is absorbed except for the green ray within 1.7–1.9cm^{-1} (525–588nm). The absorption peaks of O_2 and H_2O around 1.39 cm^{-1} (720nm), 1.31 cm^{-1} (760nm), 1.22cm^{-1} (820nm), and 1.07cm^{-1} (940nm) can be clearly acquired from both spectral curves. Figure 20(c) shows the band integrated data of DoP image. The intensities of the windows in Fig. 20(a) are lower than the building wall since the light goes through the glasses more easily. However, in the DoP image the opposite occurs because the primary specular reflection has higher Dop than that of the walls which produce diffuse reflection.

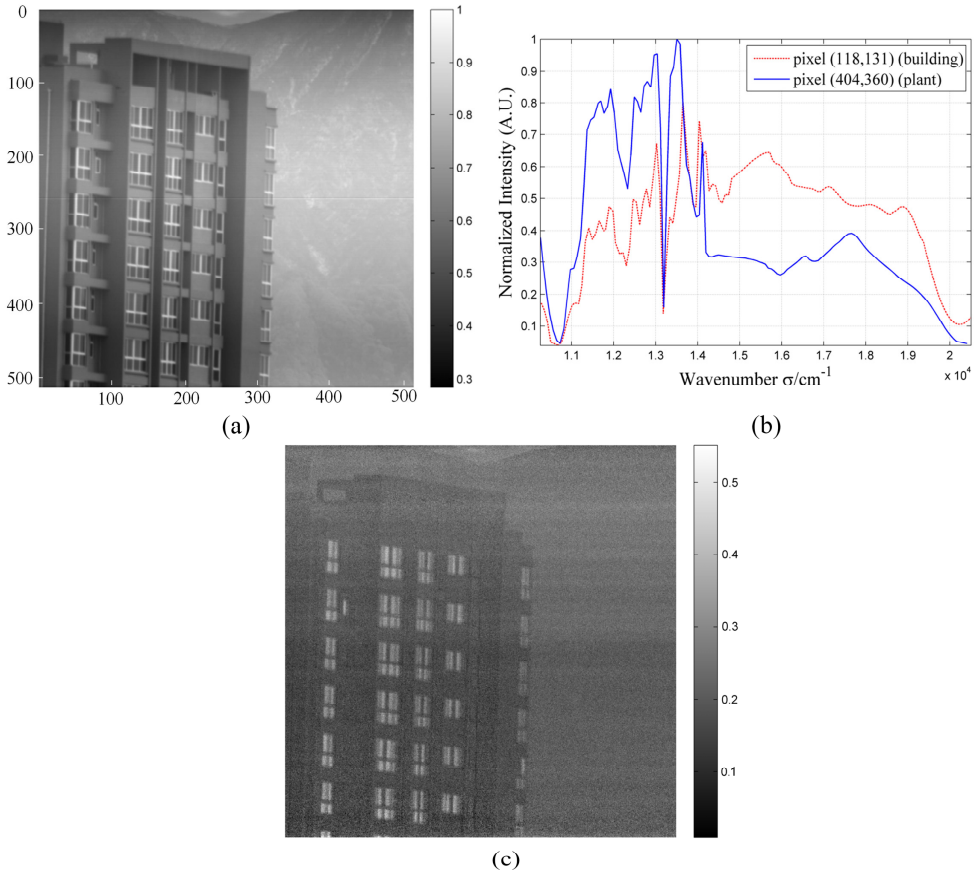

Fig. 20. Outdoor tests results. (a) S_0, band integrated data. (b) Spectra recovered at two selected pixels across the scene. (c) DoP, band integrated data.

5. Conclusion

In this paper we presented a high throughput static channeled interference imaging spectropolarimeter (CIISP) that acquires the full wavelength-dependent SOP, spectral and spatial information simultaneously. The CIISP is based on channeled polarimetry and a Savart polariscope with no internal moving parts, and employs tempo-spatially mixed modulated mode which brings a high optical throughput benefitting from the lack of the slit. Sensor calibration including spectral, radiometric and polarimetric calibration techniques was involved to ensure the detecting accuracy across the band σ = 10416.67–20833.33cm^{-1} (λ = 480–960nm). The modified polarimetric calibration method reduces the reconstructed errors via eliminating the amplitude error caused by reference beam. Laboratory experiments of

Optics EXPRESS

uniform LED and halogen lamp lights illuminating the target with a broadband polarizer demonstrated the spectropolarimetric capability of the instrument. The results of outdoor test on plants and building further proved that the system could acquire high quality spectral and spatial data of a scene, while the DoP image illustrates potential applications for target identification in low light levels. Further work on our CIISP system will include introducing an additional retarder placed between Savart polariscope and analyzer P_2, which enables a single-sided interferogram to be measured, and the thickness of the retarders R_1 and R_2 will be adjusted to produce larger optical path difference in each channel. Improving reconstruction accuracy and performing additional outdoor testing are the next step to meet the needs of spectral and polarization information in industrial and scientific fields.

Funding

National High Technology Research and Development Program of China (Grant No. 2012AA121101); Major Program of the National Natural Science Foundation of China (Grant No. 41530422); National Science and Technology Major Project of the Ministry of Science and Technology of China (Grant No. 32-Y30B08-9001-13/15); National Natural Science Foundation of China (Grant No. 61275184, 61540018, 61405153).